An Advanced Spatial Approach Based on Multi-criteria Analysis and Geostatistical Simulation for a Comprehensive Geogenic Radon Hazard Index Mapping

Iman MASOUMI, Sabrina MAGGIO, and Sandra DE IACO

Radon concentration originates mainly from geogenic factors, such as uranium content, permeability based on rock unit and tectonic features, as well as karst properties. In this paper, these layers are integrated through a joint spatial multi-criteria approach based on Analytical Hierarchy Process and Fuzzy Gamma Operator techniques, as well as on the Receiver Operating Characteristic curves in order to compare output maps and classify them to construct a Geogenic Radon Hazard Index for Lecce Province in southeastern Italy. To this end, two main criteria and their sub-criteria are defined as contributing factors: geology (uranium content in bedrock, permeability rate in different lithotypes, and faults) and karst features (dolines, caves, and sinkholes). Furthermore, the spatial multi-criteria results, also confirmed by the indoor radon maps generated through Sequential Gaussian Simulations, show that the sites rich primarily in uranium content in bedrock, faults, and sinkholes can be identified as the most critical areas. Finally, the evaluation of the performance is completed through the Success Rate Curve, which demonstrates the efficiency of the Fuzzy Gamma Operator method and corroborates that this innovative spatial multi-criteria approach can support the production of reliable maps of high radon potential areas. This approach encourages the development of effective risk reduction strategies for future planning and targeted sampling in areas with limited indoor radon data.

Key Words: Radon Hazard; Fuzzy Gamma Operator; Analytical Hierarchy Process; Sequential Gaussian Simulation.

1. INTRODUCTION

Radon maps are instrumental in identifying target areas to prevent the harmful effects of radon on people's health (Gruber et al. 2013; Čeliković et al. 2022; Dobrzyńska et al.

Iman Masoumi, National Biodiversity Future Center, Palermo, Italy.
Sabrina Maggio, Department of Economic Sciences, University of Salento, Lecce, Italy.
Sandra De Iaco (✉) National Centre for HPC, Big Data and Quantum Computing, Bologna, Italy. National Biodiversity Future Center, Palermo, Italy (E-mail: *sandra.deiaco@unisalento.it*).

Journal of Agricultural, Biological, and Environmental Statistics
https://doi.org/10.1007/s13253-024-00654-6

2023; Coletti et al. 2022). Indeed, the main purpose of producing these maps is to detect areas that feature high radon concentrations, so that in the future the necessary preventive actions might be implemented to mitigate the radon level or restrict the construction of new residential neighborhoods in these areas. Numerous studies were conducted around the world with the scope to produce radon maps (Bekteshi et al. 2017; Rezaie et al. 2022; Beldean-Galea et al. 2020; Giustini et al. 2022; Lupiano et al. 2023; Elío et al. 2023; Loffredo et al. 2022; Cori et al. 2022). Many of these surveys were aimed at drawing interpolation and extrapolation maps to quantify the radon level over the domain of interest and a variety of statistical and geostatistical methods were employed to estimate the radon levels (Elío et al. 2023; Giustini et al. 2019; Loffredo et al. 2021; Khan et al. 2019; Ciotoli et al. 2007; Durec et al. 2003). Two important factors were identified, namely generation and transportation of radon, which are directly linked to natural and geogenic sources. These factors significantly affect the concentration of radon in an area (Malmqvist et al. 1989; Nazaroff 1992). The geological properties of a place, including the type of rock with its uranium content (as the primary source of radon production) and permeability (which enables radon transfer depending on lithology type), play crucial roles in determining radon levels. Furthermore, other factors such as faults, caves, dolines and sinkholes are also recognized as significant factors and were the object of several contributions (Coletti et al. 2022; Beldean-Galea et al. 2020; Ciotoli et al. 2017; Guida et al. 2013; Petermann and Bossew 2021; Cinelli et al. 2015; Miles and Appleton 2005; De Iaco et al. 2017; Dai et al. 2019; Smethurst et al. 2017). The study in Botti et al. (2023) examines the impact of karst features on indoor radon levels, taking into account building materials and floor levels. The findings underscore the significance of karst regions, especially those which consider surface karst phenomena, in influencing indoor radon concentrations. Additionally, research outlined in Eisenlohr and Surbeck (1995) demonstrates elevated radon levels in spring waters, particularly within karstic aquifers, as evidenced by sampling and observation. Research focused on these characteristics has revealed spatial structures and geographical trends across different regions (Ciotoli et al. 2007). By considering the aforementioned factors, it is worth generating a Geogenic Radon Hazard Index (GRHI) map to assess whether an area is prone to elevated indoor radon concentrations and to identify prioritized areas for radon mitigation. This is of sure interest in order to protect public health and to preserve biodiversity, which represents the core of ecosystem.

Among the studies focused on deterministic and probabilistic methods for interpolating radon measurements and producing maps, only a few specifically addressed the construction of GRHI maps (Nazaroff 1992; Szabó et al. 2014; Giustini et al. 2021; Masoumi et al. 2024). Due to the limited availability of empirical data, such as indoor radon measurements and permeability, the initial efforts to introduce GRHI maps were done by Friedmann et al. (2017); subsequently, further research proposed advances in the methodology in this field (Giustini et al. 2021; Petermann et al. 2021). In the production of GRHI maps, the use of different predictors has always represented a challenge due to the potential inconsistency between neighboring regions. To ensure accurate results, it is crucial to have an appropriate distribution and density of input data, as highlighted in Bossew et al. (2020). In the latest study conducted in the Lecce province (Italy), the radon potential was investigated by applying the Regression–Kriging method using various parameters such as geology, faults, karst, permeability as covariates, along with radon soil gas measurements (De Iaco et al. 2017). Moreover, based on the findings of Gruber et al. (2013), this area does not show a hazard risk of radon, although there are some local areas that deserve attention.

Thus, the absence of a GRHI map in Lecce province, coupled with the presence of geology and karst features related to high radon hazard areas, on the one hand, and the need of an advanced spatial approach for generating reliable maps have motivated the present investigation. The main objectives are threefold (i) to propose an innovative radon mapping procedure which implements spatial multi-criteria decision analysis (SMCDA) and Sequential Gaussian Simulation (SGS) methods; (ii) to prioritize high radon hazard areas based on geogenic factors such as geology and karstic features, using SMCDA based on the use of Analytical Hierarchy Process (AHP) and Fuzzy Gamma Operator (FGO) methods; (iii) to compare and evaluated the results with an E-type map generated through SGS for indoor radon sampling measurements. Through the SMCDA approach, a concise, integrated and informative map of high radon hazard areas in Lecce Province has been created based on geology and karstic features criteria. Note that although the SMCDA approach for producing GRHI maps was used in a few studies, in this paper it has been further enhanced by classifying the final GRHI maps into distinct classes of radon potential via the so-called Receiver Operating Characteristic (ROC) curve method, and the suitable γ value has been chosen according to the calculated Area under the Curve (AUC). Thus, it is shown how the integration of expert knowledge and statistical methods enables the identification of the most prioritized criteria in generating GRHI maps, offering a significant advantage.

It is worth pointing out that this study provides a discussion on the spatial relationship among radon potential factors and an accurate GRHI map from FGO outputs, which are also compared through the E-type map. This last map has been generated by simulating 100 sequential gaussian realizations, conditional on some available indoor radon sampling measurements. A comparison between the two output maps, obtained from two different methods (AHP-FGO and SGS), has been based on the Success Curve Rate (SCR). By addressing the absence of a GRHI map, thanks to the integration of various geogenic factors through a well-structured methodology, this investigation seeks to provide valuable insights into high radon hazard areas and offer a reliable tool for future decision-making processes.

2. STUDY REGION AND COLLECTED DATA

The area of interest is the Lecce Province, which is situated in a southern region of Italy and spans approximately 2765 square kilometers (Fig. 1).

Its population counts 800000 residents, with the majority concentrated in the central part of the province. Except for the northern part, which is bordered by land, the other parts of Lecce province are surrounded by the sea; moreover, this territory is characterized by a geologically intricate landscape and a complex structural arrangement. Thus, the incorporation of layers representing lithological uranium content and factors influencing the sub-surface transfer of radon, such as permeability, faults, and karst features, is crucial. Indeed, these layers have been considered in this study as significant geogenic sources

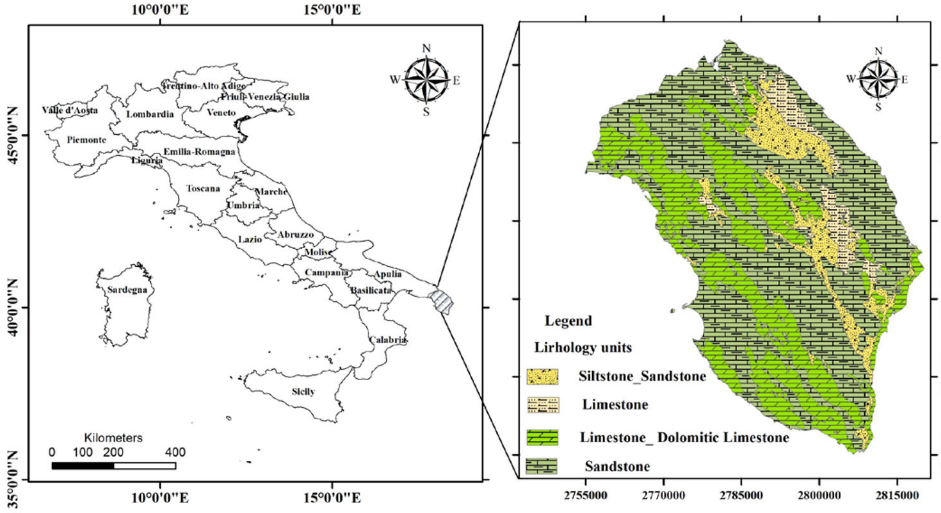

Figure 1. Location map and geological map of the Lecce province.

which contribute to the generation and transfer of radon. According to the Italian national maps, Lecce Province represents a low hazard area for radon, but on the other hand there are certain localized anomalies in the radon potential which deserve attention (Sciocchetti et al. 1985). It is worth noting that, based on the kind of lithology and also its history during geological cycles, the uranium content is different in various kinds of lithology (plutonic, volcanic, metamorphic, and sedimentary).

Figure 1 shows four main lithotypes, from the Cretaceous period in this province, including sandstone, limestone, dolomite–limestone, and siltstone–sandstone. Additionally, the region is covered by clay, sand, and silt deposits from the Miocene and Quaternary periods (Tulipano and Fidelibus 2002). Drawing upon the studies (Nogarotto 2018; Taroni et al. 2010) and the outcomes of mapping the uranium content in Italy's bedrock, these lithological units were classified into high uranium content in limestone and dolomitic limestone and low uranium content in sandstone. This categorization serves to investigate the relationship between lithology type and uranium concentration, which acts as the primary source of radon generation. The permeability of lithotypes in sedimentary rocks and the comparison between them is described in Domenico and Schwartz (1997), Allen and Allen (2013). Based on these sources and considering different lithological types in Lecce Province, the areas mainly composed of limestones and dolomitic limestones are identified as having high permeability due to numerous fractures and faults. Conversely, the eastern region, dominated by siltstone–sandstone lithotypes, exhibits low permeability due to the presence of silt. The remaining areas, characterized by sandstone lithotypes, show moderate permeability.

Moreover, the presence of faults plays a significant role in this area and previous research indicates a general correlation between morphology and tectonic activity (Caramanna et al. 2008; Festa et al. 2015). The morphological characteristics are influenced by the presence of numerous karstic features, particularly sinkholes that have mainly developed in the Pleistocene calcarenite (Lupiano et al. 2023). The scarcity of surface water also contributes to the

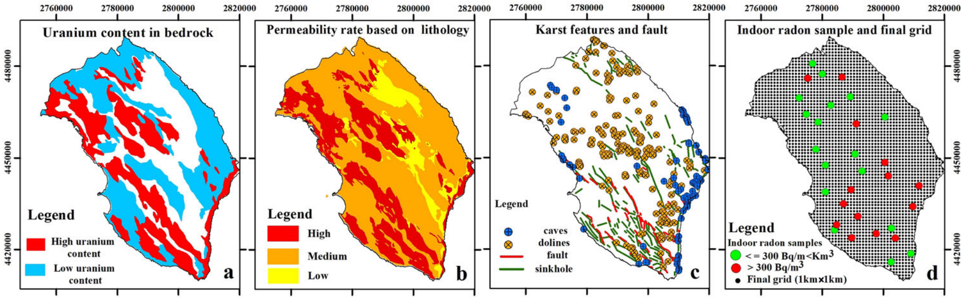

Figure 2. **a** Uranium content in bedrock (Nogarotto 2018), **b** Permeability rate (De Iaco et al. 2017; Domenico and Schwartz 1997; Allen and Allen 2013), **c** faults and karst features (https://www.isprambiente.gov.it/it, http://www.sit.puglia.it), **d** sampling indoor radon locations with regular grid in Lecce province (ISPESL).

formation of karsts and the fragmentation of rocks; furthermore, the aquifer is composed of fractured and karstified limestones and dolomitic limestones (Leucci et al. 2004). Various types of karst features, such as caves, sinkholes, and dolines, equally affect the movement and transportation of radon, in addition to the aforementioned factors. The detection of changes in radon concentration is observed in regions characterized by high fracturing and cracking, as well as in areas where lithological variations result in different permeability levels.

In this study, various important layers have been categorized into two major groups: geology and karst features. Then these layers, provided by the Lecce province, ISPRA (Higher Institute for Environmental Protection and Research) and SIT APULIA, have been integrated to identify radon hazard areas. Furthermore, data from indoor radon measurements collected at 30 sites in 2006 by ISPESL (Higher Institute for Prevention and Safety at Work) and well distributed throughout the study region, have also been used in the analysis. For the entire area, a regular square grid with cells of (1 km x 1 km) has been established and utilized for both the FGO and SGS methods.

Figure 2 displays the classification of uranium content in various lithologies bedrock (Nogarotto 2018; Taroni et al. 2010), the permeability rate in different lithology types (De Iaco et al. 2017; Domenico and Schwartz 1997; Allen and Allen 2013), and the incidence of faults and different types of karst features. Additionally, it indicates the locations of indoor radon sampling measurements in Lecce Province, depicted within the regular grid used for this study.

As previously clarified, the input layers used to produce the GRHI map in Lecce province are divided into two major criteria, which include geology and karst features, each with their respective sub-criteria. In addition to these data, 30 sample indoor radon concentrations collected by ISPESL in 2006 have also been utilized for simulation purposes. The final maps have been generated, analyzed, and compared by processing all layers and data through the Geographic Information System QGIS and the Stanford Geostatistical Modeling Software SGeMS.

3. METHODOLOGY

The AHP-FGO and SGS methods employed for mapping high radon potential regions are described in this section. Figure 3 outlines the methodological flowchart used in this study. The AHP-FGO method starts with the definition of distinct indicator criteria, followed by the assessment of their importance using the AHP technique. FGO is then applied to fuzzy layers based on various γ values, and the ROC method is employed to categorize maps in different classes; subsequently, the best γ value has been chosen on the basis of the AUC values, as comprehensively described in Sects. 3.1, 3.2, and 3.3. The SGS method discussed in Sect. 3.4, is utilized to generate E-type and probability maps. Finally, Sect. 4 provides a comparative analysis between these two maps on the basis of the SCR.

3.1. AHP

The AHP was introduced in the 1970s by Saaty (1977) and used as a practical, simple, flexible, and easy method in various applications in engineering, industry, management, sports (Saaty 1977; Zhang et al. 2015; Chen and Huang 2013; Eitvandi et al. 2022; Hsu et al. 2008; Saaty and Vargas 2013; AlFanatseh 2022; Motiee et al. 2023).

The methodology comprises the following steps:

- Define the criteria and sub-criteria
- Implement the pairwise comparison matrix and check the judgments
- Calculate the weights of criteria based on expert knowledge and literature
- Apply the sensitivity analysis to check the results.

After defining the criteria and sub-criteria necessary to achieve the study's goal, the prioritization of various influential criteria and sub-criteria has been fixed through a pairwise comparison matrices, as illustrated below (Hsu et al. 2008):

$$A = [a_{ij}] = \begin{array}{c} \\ C_1 \\ C_2 \\ \vdots \\ C_n \end{array} \begin{array}{c} \begin{array}{cccc} C_1 & C_2 & \cdots & C_n \end{array} \\ \begin{bmatrix} 1 & a_{12} & \cdots & a_{1n} \\ 1/a_{12} & 1 & \cdots & a_{2n} \\ \vdots & \vdots & \ddots & \vdots \\ 1/a_{1n} & 1/a_{2n} & \cdots & 1 \end{bmatrix} \end{array} \tag{1}$$

where $C_1, C_2, \ldots, C_n$ are the set of criteria and sub-criteria and a_{ij} represents the judgment according to the scale described in Table 1. The outcomes obtained by comparing the criteria and sub-criteria are incorporated into the pairwise comparison matrix, denoted as A. The elements below the diagonal are the reciprocals of the corresponding values of the upper triangular matrix. Specifically, for a given pair of criteria or sub-criteria (C_i, C_j), with $i, j = 1, 2, \ldots, n$, $i \neq j$, the single value a_{ij} is provided, then the relative judgment for the inverse comparison (C_j, C_i) becomes $a_{ji} = 1/a_{ij}$ (Hsu et al. 2008).

Table 1. Priority scale between two criteria or sub-criteria in the AHP

Factors intensity	Description (for any pair of objectives i, j)	Intensity degree of importance
1	The two factors have an identical objective	Equal
3	A factor is prioritized marginally against another	Moderate
5	A factor is highly prioritized against another	Strong
7	A factor is prioritized very strongly against another and it is demonstrated in action	Very strong
9	The proof for prioritizing one factor against another has the highest possible strength to validate	Extreme
2, 4, 6, 8	Deployed to show the compromises between the preference scores 1, 3, 5, 7 and 9	Intermediate value between two adjacent judgments
Reciprocal	Deployed to do inverse comparisons	Opposites

Alternatively, if a collection of numerical weights $W_1, W_2, \ldots, W_n$ is associated with the n criteria or sub-criteria $C_1, C_2, \ldots, C_n$, respectively, the entries of the consistency matrix A can be straightforwardly derived by assuming the relationship between the weights W_i and the assessments a_{ji} such that $\frac{W_i}{W_j} = a_{ij}$ (for i, j = 1, 2,…, n); thus, the matrix A is outlined as follows:

$$A = \begin{array}{c} \\ C_1 \\ C_2 \\ \vdots \\ C_n \end{array} \begin{array}{c} \begin{array}{cccc} C_1 & C_2 & \cdots & C_n \end{array} \\ \begin{bmatrix} w_1/w_1 & w_1/w_2 & \cdots & w_1/w_n \\ w_2/w_1 & w_2/w_2 & \cdots & w_2/w_n \\ \vdots & \vdots & \ddots & \vdots \\ w_n/w_1 & w_n/w_2 & \cdots & w_n/w_n \end{bmatrix} \end{array} \quad (2)$$

As suggested in Saaty and Vargas (2013), the largest eigenvalue λ_{max} is computed from this matrix, so that it is employed to assess the consistency index (CI) and consistency ratio (CR) of the comparison matrix, as defined below:

$$CI = \frac{\lambda_{max} - n}{n - 1} \quad (3)$$

$$CR = \frac{CI}{RI} \quad (4)$$

where RI is the random consistency index, which serves as a measure of the average randomness in the ranking of attributes based on various pairwise comparisons. In Table 2, the RI values for different values of n are shown. If the computed CR is equal to or less than 10% (0.10), it indicates that the assessment of attribute importance is reliable, and any inconsistencies can be disregarded (Hsu et al. 2008; Saaty and Vargas 2013). On the

Table 2. Values for the random consistency index RI, given the matrix order n (Saaty and Vargas 2013)

n	1	2	3	4	5	6	7	8	9	10
RI	0	0	0.53	0.9	1.12	1.24	1.32	1.41	1.45	1.49

other hand, a CR value greater than 10% suggests that the comparisons lack of consistency, necessitating corrections to the judgments in the matrix, as highlighted by Saaty and Vargas (2013).

Once the weights of the criteria and sub-criteria have been determined, the following equation is employed to calculate the final score of each sub-criterion:

$$S_{ij} = (Wf_j \times Wc_{ij}) \tag{5}$$

where S_{ij} indicates the final score of each sub-criterion i within the criterion j, W_{fj} indicates the weight of criterion j, and Wc_{ij} indicates the weight of sub-criterion i within criterion j. This calculation has been applied for $j = 1 \ldots, n_c$ and $i = 1, \ldots n_j$ where n_c is the number of criteria and n_j is the number of sub-criteria for each criterion j (Eitvandi et al. 2022).

In this study, the hierarchical structure has been initially established based on two main factors, namely, geology ($j = 1$) and karst features ($j = 2$), which represent the criteria used to explore radon hazard areas in the study region. They contain six and three sub-criteria, respectively, as shown in Fig. 3.

Using inputs from various expert judgments and a thorough review of articles and technical documents related to the subject, scores have been assigned to prioritize the factors (Coletti et al. 2022; Ciotoli et al. 2017; De Iaco et al. 2017; Eisenlohr and Surbeck 1995; Nogarotto 2018; Ciotoli et al. 2020). Subsequently, based on the expertise of decision-makers, a pairwise comparison matrix has been created for the two main criteria and nine sub-criteria at each hierarchical level to determine the final weights, as in Eqs. (1) or (2). For instance, according to Table 3, the factor intensity of geology in relation to the karst features has been considered as 2 (based on the scale in Table 1). Then, the pairwise comparison matrix has been normalized by calculating the sum of each column (equal to 1.5 for geology and equal to 3 for karst feature) and dividing each element in a column by the sum. Subsequently, the weights Wf_j have been calculated based on the average of each row for both geology and karst features, resulting in 0.667 and 0.333, respectively.

According to Table 4, the factor intensities of sub-criteria within geology ($j = 1$) and karst features ($j = 2$) have been determined. In the geology main criterion, the sub-criteria include high uranium content in bedrock (c_{11}), low uranium content in bedrock (c_{21}), high permeability (c_{31}), medium permeability (c_{41}), low permeability (c_{51}), and fault (c_{61}). For karst features, the sub-criteria are cave (c_{12}), sinkhole (c_{22}) and doline (c_{32}). The judgments of these sub-criteria, denoted in (1) as a_{ij} (with $i = 1, 2, \ldots, 6$ and $j = 1$ for geology, $i = 1, 2, 3$ and $j = 2$ for karst features), are given in Table 4. For example, the pairwise comparison matrix for geology sub-criteria has been normalized by calculating the sum of each column (e.g., for c_{11}, the column sum is equal to 2.365) and dividing each element in

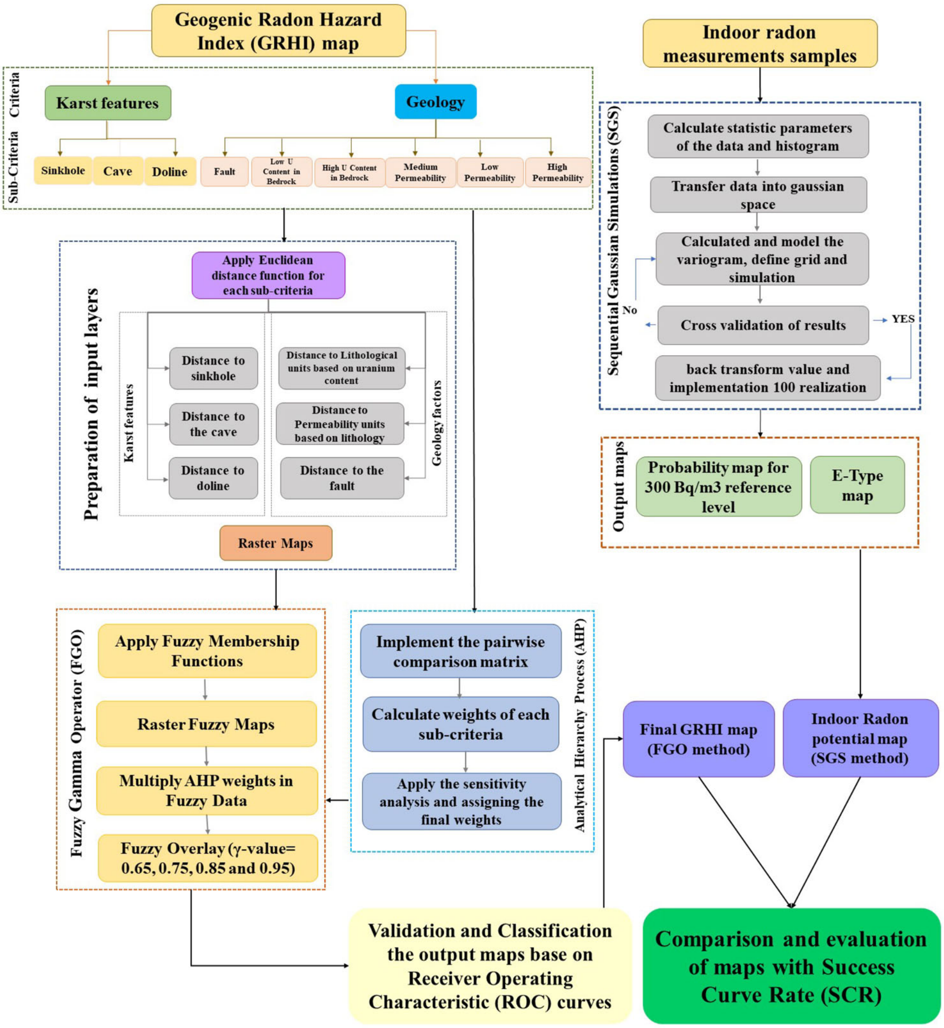

Figure 3. Overview of the study process.

a column by the sum. Subsequently, the weights Wc_{ij} have been calculated based on the average of each row for the sub-criteria. For fault as indicated a_{61} in Table 4, this normalization and averaging resulted in a weight of 0.219 (Wc_{61}). The same process has been done for the other sub-criteria related to two main criteria and results presented for the nine sub-criteria in two main criteria group in Table 4. The CR values, calculated based on Eq (3) and (4), are less than 10%, indicating consistent pairwise comparisons. These results substantiate the accuracy of the parameter ratings and weights (Saaty 1977). Finally, by utilizing the provided weights (Wc_{ij} and W_{fj}) and applying Eq. (5), the final scores (S) of each sub-criterion have been determined, as reported in Table 4. Based on the results, the most appropriate sub-criteria affecting radon potential are ranked as follows: high uranium content in bedrock (0.277), sinkholes (0.164), fault (0.146), high permeability (0.138),

Table 3. Comparison matrix and weights (W_{fj}) of the main criteria according to AHP method

Main criteria	Geology	Karst Features	Wf_j
Geology	1	2	0.667
Karst Features	0.50	1	0.333
Consistency ratio	0.001		

doline (0.104), cave (0.065), medium permeability (0.056), low permeability (0.025), and low uranium content in bedrock (0.024).

Note that various weights for geology and karst features (from 0.1 to 0.9, with step 0.1) have been also considered to examine how much the changes in weights affect the ranking of sub-criteria. The heatmap plot in Fig. 4 demonstrates the rank changes of each sub-criteria across nine different scenarios, providing a clear comparison of their performance. Based on the average ranks and standard deviations shown in the last two columns of Table 4, most sub-criteria exhibit robustness and stability when compared to their current ranks (associated with the weights for geology and karst features equal to 0.667 and 0.333, respectively). High uranium content and sinkhole consistently maintain high rankings with low to moderate variability, reflecting their significant impact in the analysis. Conversely, low uranium content and low permeability remain consistently low-ranked with minimal sensitivity to weight changes, indicating a lesser influence on the overall ranking. Sub-criteria such as cave and doline display higher standard deviations, suggesting more sensitivity to weight variations and necessitating careful consideration in decision-making processes. Overall, the analysis highlights the relative stability of most sub-criteria, with a few showing significant variability under different weighting scenarios. Considering a tolerance of 15% around main criteria weights 0.667 and 0.333 (as highlighted by the red rectangle in Fig. 4), it should be noted that the assigned final weights, based on expert knowledge, do not significantly alter the sub-criteria rankings compared to their current ranks in Table 4.

3.2. FGO METHOD

Fuzzy logic modeling was first introduced by Zadeh (1965). In the context of fuzzy set theory, a value within the range of [0, 1] is assigned to every instance (object, numerical measurement value, factor) according with its degree of belonging to specific sets. Each instance has the potential to belong to multiple sets with differing membership values. This characteristic proves highly influential in the realms of data classification and decision-making, yielding dependable and precise outcomes. The assignment of membership values is accomplished through a membership function, which transforms all provided elements into values ranging from 0 to 1:

$$A = \{(x, \mu_A(x)) \mid x \in X\} \tag{6}$$

$$\{\mu_A(x) \mid x \in X\} \rightarrow [0, 1] \tag{7}$$

Table 4. Weights, scores, and ranks of the sub-criteria according to AHP (Wc_{ij} is the weight of a sub-criterion, and S is the final score of a sub-criterion)

Criteria	Sub-criteria (c_{i1})	c_{11}	c_{21}	c_{31}	c_{41}	c_{51}	c_{61}	Wc_{ij}	S	Current rank	Average rank	Rank standard deviation
Geology (j=1)	c_{11}	1	9	2	7	9	2	0.415	0.277	1	2.33	1.41
	c_{21}	0.111	1	0.2	0.333	1	0.142	0.036	0.024	9	8.77	0.66
	c_{31}	0.5	5	1	3	5	1	0.207	0.138	4	4.88	1.26
	c_{41}	0.143	3	0.3	1	3	0.333	0.084	0.056	7	6.33	1.11
	c_{51}	0.111	1	0.2	0.333	1	0.2	0.038	0.025	8	7.77	0.66
	c_{61}	0.5	7	1	3	5	1	0.219	0.146	3	3.66	1.41
	Consistency ratio	0.014										
Karst features (j=2)	Sub-criteria (c_{i2})	c_{12}	c_{22}	c_{32}				Wc_{ij}	S	Current rank	Average rank	Rank standard deviation
	c_{12}	1	0.5	0.5				0.196	0.065	6	5.33	2.17
	c_{22}	2	1	2				0.493	0.164	2	2.11	1.53
	c_{32}	2	0.5	1				0.311	0.104	5	3.77	2.16
	Consistency ratio	0.056										

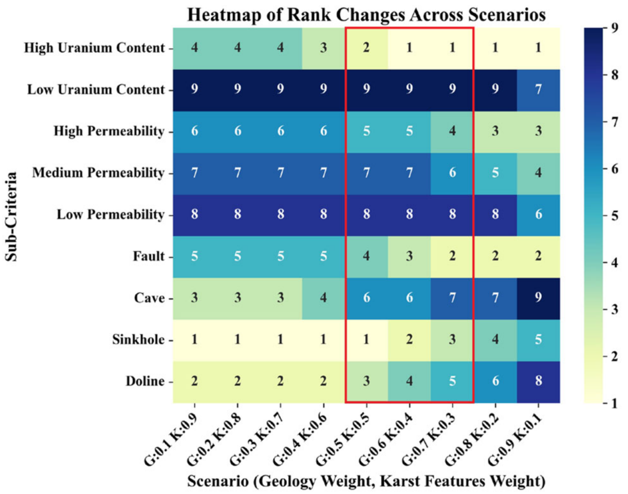

Sub-Criteria	G:0.1 K:0.9	G:0.2 K:0.8	G:0.3 K:0.7	G:0.4 K:0.6	G:0.5 K:0.5	G:0.6 K:0.4	G:0.7 K:0.3	G:0.8 K:0.2	G:0.9 K:0.1
High Uranium Content	4	4	4	3	2	1	1	1	1
Low Uranium Content	9	9	9	9	9	9	9	9	7
High Permeability	6	6	6	6	5	5	4	3	3
Medium Permeability	7	7	7	7	7	7	6	5	4
Low Permeability	8	8	8	8	8	8	8	8	6
Fault	5	5	5	5	4	3	2	2	2
Cave	3	3	3	4	6	6	7	7	9
Sinkhole	1	1	1	1	1	2	3	4	5
Doline	2	2	2	2	3	4	5	6	8

Figure 4. Ranking stability of sub-criteria across different weight scenarios of main criteria (G and K are geology and karst features weights, respectively, in horizontal axis).

$\mu_A(x)$ characterizes the membership function, while A denotes a collection of elements. As a result, for every x belonging to A, $\mu_A(x)$ indicates to what extent the element x is part of the set A (Kelley 2009). The application of fuzzy logic modeling for producing the final map is generally implemented in three steps: (a) fuzzification of the data, (b) using logical operators for integration, and (c) defuzzification of the output maps for interpretation (Kelley 2009; Sekandari et al. 2020).

First, all spatial information is regarded as crisp data (data with distinct values). To transform the available data into fuzzy data, the initial preparation phase involves creating separate distance maps for each adopted criterion. These distance maps rely on the Euclidean distance method, which measures the shortest distance from each cell (or pixel) in the output raster to the nearest edge of any polygon in the input layer using QGIS software.

The methodology has been applied to all vector files containing nine sub-criteria, resulting in a total of nine distinct distance maps. For example, when assessing high or low uranium bedrock, the Euclidean distance method generates a raster map where each cell's value represents the shortest distance to the nearest boundary of a high or low uranium bedrock zone in Fig. 5b, c. Following this, the input data have been normalized in order to obtain values in the range from 0 to 1. To achieve this goal, the fuzzy logic extension of QGIS software offers various fuzzy membership functions, including those that generate a sigmoid-shaped membership, which is a commonly utilized feature across numerous fuzzy membership applications (Raines et al. 2010). In this study, the small and large fuzzy membership functions according to the relationship of each criterion with the goal of this analysis, i.e., mapping hazard radon areas, have been used to convert the values of different layers into the [0–1] range. The small fuzzy membership function, given in Eq. (8), is used when smaller input values carry more significance, resulting in higher membership values (Raines et al. 2010). This function highlights the probability of incorporating smaller input values into the set. Indeed, through this function, values below the midpoint receive increased emphasis. On the other hand, the large fuzzy function, introduced by Raines et al. (2010) and Mohebbi Tafreshi et al. (2021), is utilized for emphasizing large input values. In particular, through this function, values exceeding the midpoint are highly likely to be part of the set, whereas values below the midpoint have a lower probability of being included. This function, given in Eq. (9), enhances membership values above the midpoint. As specified in Raines et al. (2010), the following equations formally define the small and large membership functions:

$$\mu\,(\mathrm{x}) = \frac{1}{1+\left(\frac{\mathrm{x}}{\mathrm{f}_2}\right)^{\mathrm{f}_1}} \tag{8}$$

$$\mu\,(\mathrm{x}) = \frac{1}{1+\left(\frac{\mathrm{x}}{\mathrm{f}_2}\right)^{-\mathrm{f}_1}} \tag{9}$$

where $\mu(\mathrm{x})$ represents the membership value of the category, while f_1 and f_2 denote the spread and midpoint values, respectively.

Given that sub-criteria such as high uranium bedrock, high and medium permeability, and all karst features in close distance have a significant impact on radon hazard areas, a small function has been employed. For the remaining two sub-criteria, which involve low uranium content in bedrock and low permeability with an inverse relationship to distance from the target, a large function has been applied. In Fig. 5, the standardization of high and low uranium content in bedrock, using fuzzy small and large function, has been shown. By applying the fuzzy membership functions to all seven other sub-criteria, the generation of final fuzzification maps has been accomplished, as illustrated in Fig. 6.

After standardizing each of the sub-criteria that affect radon potential, they have to be combined. Before combining the layers, the scores from each sub-criterion, as calculated by the AHP method and presented in Table 4, are multiplied by each fuzzy layer.

The fuzzy logic method employs five operators (fuzzy gamma, fuzzy AND, fuzzy algebraic sum and product, fuzzy OR) with the purpose to overlay all layers. The two most used operators in combination with fuzzy membership function are AND and OR. However, they have their drawbacks. The OR operator yields the maximum value as output, while the AND operator gives the minimum value. To overcome these limitations, fuzzy algebraic sum, fuzzy algebraic product and FGO are employed for combining data. Fuzzy algebraic product and fuzzy algebraic sum define the outputs as follows:

$$\mu_{\mathrm{p}}(\mathrm{x}) = \prod_{\mathrm{i}=1}^{\mathrm{n}} \mu_{\mathrm{i}}(\mathrm{x}) \tag{10}$$

$$\mu_{\mathrm{s}}(\mathrm{x}) = 1-\prod_{\mathrm{i}=1}^{\mathrm{n}} (1-\mu_{\mathrm{i}}(\mathrm{x})) \tag{11}$$

In Eqs. (10) and (11), n denotes the number of membership functions intended for merging and μ_{i} stands for the ith membership function. The outcome produced by the fuzzy algebraic product function is equal to or smaller than the provided minimum, while the result of the fuzzy algebraic sum function surpasses all inputs but never exceeds 1. As in Eitvandi et al.

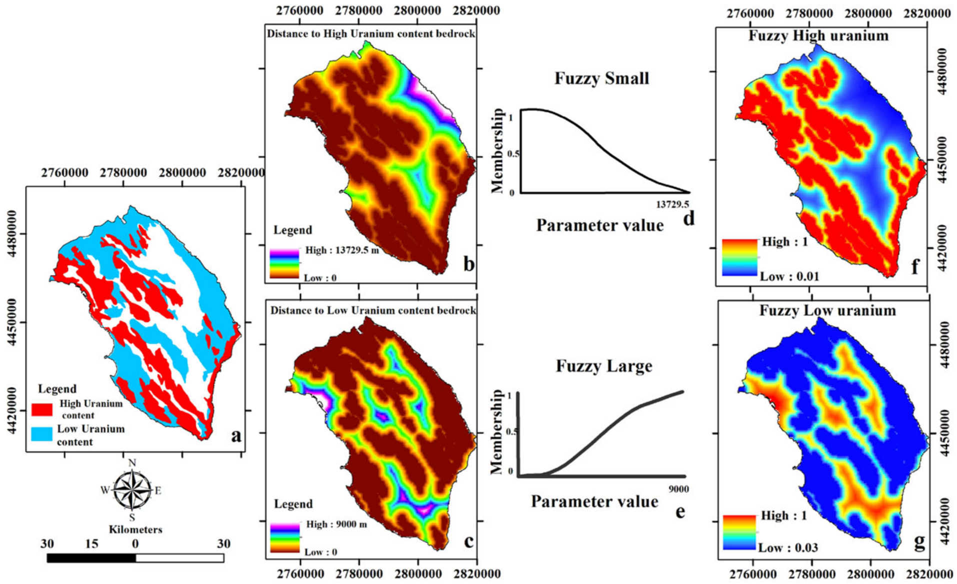

Figure 5. Fuzzy standardization of the distance to high and low uranium content in bedrock, **a** Initial layers of uranium content in bedrock, **b** and **c** Distance maps to high and low uranium content in bed rock, **d** and **e** fuzzy small and large functions, **f** and **g** Fuzzy high and low uranium maps.

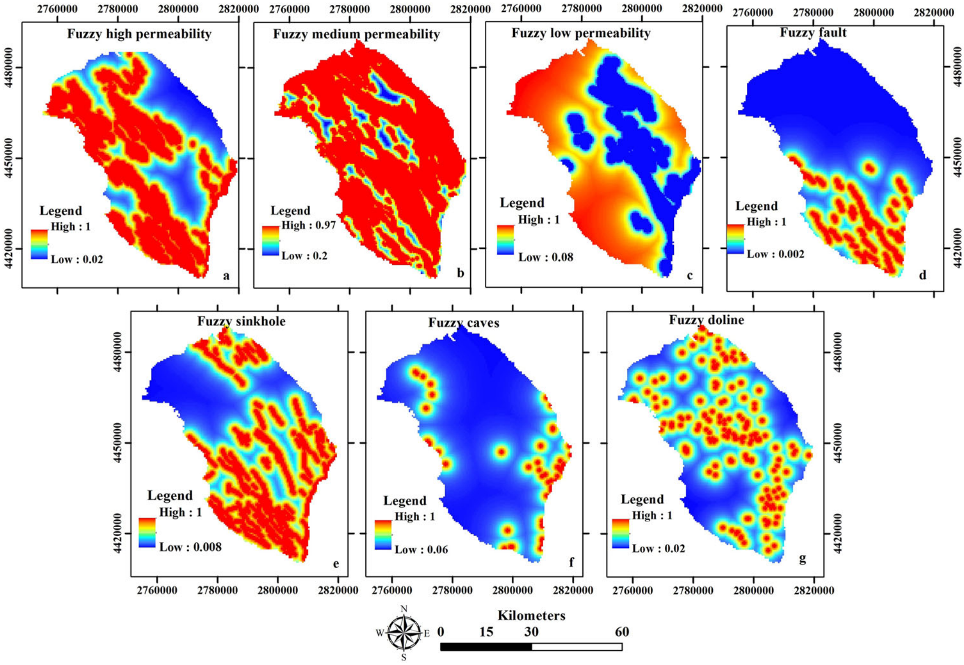

Figure 6. Fuzzy maps of sub-criteria, **a** high permeability, **b** medium permeability, **c** low permeability, **d** fault, **e** sinkholes, **f** cave, **g** doline.

(2022), the calculation of FGO is determined using Eq. (12):

$$\mu_{\gamma}\ (\mathrm{x}) = [\mu_{\mathrm{s}}\ (\mathrm{x})\ ]^{\gamma} \times [\mu_{\mathrm{p}}\ (\mathrm{x})\ ]^{1-\gamma} \tag{12}$$

where the γ-value is required to fall within the range of [0, 1] to optimize the membership fusion, so that the outcome of the fuzzy gamma, denoted as $\mu_{\gamma}(\mathrm{x})$, is determined. When γ is set to 1, the fusion is equal to the fuzzy algebraic sum, whereas for a γ value equal to 0, the fusion is reduced to the fuzzy algebraic product. If γ is chosen accurately, it results in output values that establish a balance between the additive impact tendencies of the fuzzy algebraic sum and the fuzzy algebraic product (Lewis et al. 2014). Since the value of γ can be chosen by the user, this study employs various γ values to generate final GRHI maps, which are subsequently compared to determine the most suitable one.

3.3. Validation and Verification of FGO Maps

Modeling is a crucial step for evaluating natural hazards (Nefeslioglu et al. 2013) as well as the consequent validation. Therefore, after GRHI maps have been generated, the accuracy of these maps has been evaluated with independent data that have not been used during the GRHI map creation process. Specifically, 30 sampling measurements, which were not utilized in the GRHI mapping process, have been used to evaluate the reliability of the final GRHI maps based on FGO method and then independently employed in the SGS method (Sect. 4). According to Article 103 of Directive 2013/59/EURATOM (BSS), the reference level for identifying high indoor radon areas, based on the percentage sampled measurements exceeding 300 Bq/m^3, is established at 15%. The World Health Organization recommends a reference level from 100 Bq/m^3 to 300 Bq/m^3 for dwelling; similarly, the International Commission for Radiological Protection also suggests a level equal to or less than 300 Bq/m^3 (Angell 2009; International Commission on Radiological Protection 1994; Clement et al. 2010). In this research, based on the threshold 300 Bq/m^3, the 30 samples have been classified into two different classes as follows, which are shown on the map by green and red circle points.

- Low concentration: samples with indoor radon concentration lower than 300 Bq/m^3.
- High concentration: samples with radon concentration greater than 300 Bq/m^3.

The final FGO maps of the indoor radon potential have been validated using existing the indoor radon sample data.

A ROC curve is an analytical technique, as explained in Nahm (2022) and Roumeliotis et al. (2024), which provides a graphical tool for quantifying the performance of a process. The following confusion matrix D is fundamental for evaluating the performance of classifiers and computing the integral of the ROC curves (Giglioni et al. 2021):

$$\mathrm{D} = \begin{bmatrix} \mathrm{TP} & \mathrm{FP} \\ \mathrm{FN} & \mathrm{TN} \end{bmatrix} \tag{13}$$

where

- TP stands for True Positive, that is, number of instances of true values (from samples) identified correctly by the model (Eq. 12)
- FP stands for False Positive, that is, instances incorrectly classified as positive
- TN stands for True Negative, that is, correctly identified negative instances
- FN stands for False Negative, that is, instances incorrectly classified as negative

Thus, the true positive rate (TPr), also referred to as sensitivity (SE) or the probability of detection, quantifies the proportion of correctly identified positive instances among all actual positive samples; conversely, the false positive rate (FPr), also known as the probability of false alarms, indicates the proportion of incorrectly identified positive instances among all actual negative samples (Giglioni et al. 2021):

$$\mathrm{TPr} = \mathrm{Sensivity}(\mathrm{SE}) = \frac{\mathrm{TP}}{\mathrm{TP} + \mathrm{FN}} \tag{14}$$

$$\mathrm{FPr} = 1 - \mathrm{Specifity}(\mathrm{SP}) = \frac{\mathrm{FP}}{\mathrm{FP} + \mathrm{TN}} \tag{15}$$

The ROC curve can be constructed by plotting the TPr against the FPr for different threshold values of the estimated model based on Eq. (12). It should be noted that as the curve approaches the upper left corner of the ROC space, the model's accuracy increases, but the model's accuracy decreases as the curve approaches the 45-degree diagonal line in the ROC space.

The accuracy of the model is assessed from the ROC curve by computing the Area Under Curve (AUC), defined as

$$\mathrm{AUC} = \int_0^1 \mathrm{ROC}\,(\mathrm{f})\,\mathrm{df} \tag{16}$$

where f is the FPr, while ROC(f) denotes the corresponding TPr. If the model fails to identify a radon hazard area, the AUC becomes equal to or lower than 0.5. The AUC value ranging from 0.5 to 1 indicates the performance of a model, with higher values suggesting better discrimination between two classes, as highlighted by Nahm (2022), Fawcett (2006).

Figure 7 depicts the ROC curves, drawn for various γ values. Then, the AUC values of 0.44, 0.53, 0.79, and 0.90 have been computed according to the γ values of 0.65, 0.75, 0.85, and 0.95, respectively. Notably, the first two γ values are deemed unacceptable, while among the latter two, the γ value equal to 0.95 yields the highest AUC value.

The optimal threshold value has been determined using the Youden index (Youden 1950), which measures the orthogonal distance between the ROC curve and the diagonal line, as detailed in Roumeliotis et al. (2024). This index is a valuable metric for identifying the threshold that optimally balances SE and SP. The Youden index is calculated as the sum of SE and SP minus 1 (or equivalently SE+SP-1=SE-(1-SP)=TPr-FPr), with the point having the highest index value providing the optimal classification threshold. Table 5 presents the results for FGO models, highlighting the optimal threshold points and their corresponding maximum Youden index values. These thresholds have been utilized to classify the final GRHI maps, as illustrated in Fig. 8.

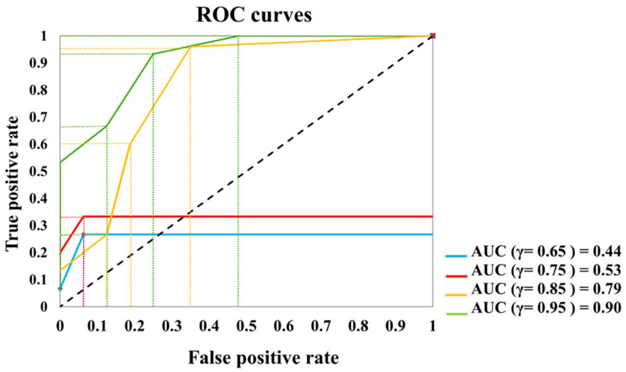

Figure 7. Evaluation of ROC curves for the four γ values.

Table 5. Optimal thresholds based on Youden index for differentγ values in corresponding FPr and TPr values

γ value	FPr (or 1-SP)	TPr (or SE)	Optimal thresholds
0.65	0.04	0.28	0.24
0.75	0.04	0.35	0.31
0.85	0.36	0.94	0.58
0.95	0.24	0.92	0.68

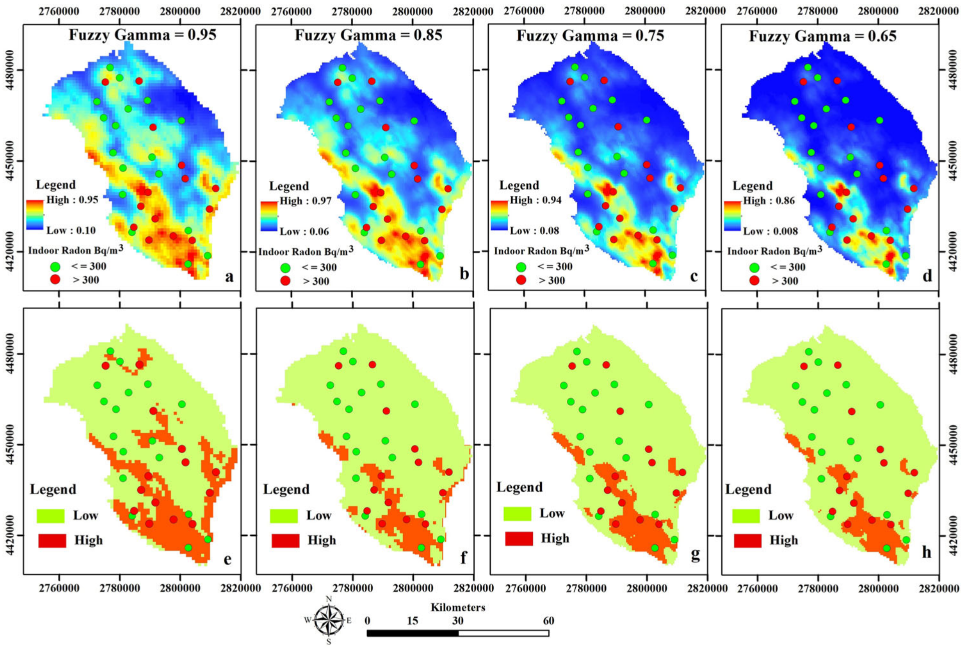

Figure 8. GRHI maps of the study region, **a** Fuzzy map for γ value 0.95, **b** Fuzzy map for γ value 0.85, **c** Fuzzy map for γ value 0.75, and **d** Fuzzy map for γ value 0.65, respectively. Corresponding classifications of each map are shown in **e**–**h**.

3.4. SGS

Geostatistical simulation techniques provide useful tools for creating numerous equally probable realizations of a spatial feature, which are instrumental in assessing the uncertainty inherent in the resulting patterns. In the literature, there are a wide range of methodologies for spatial stochastic simulation and their application has been proven in many cases in environmental and industrial projects (Buttafuoco et al. 2010; Park et al. 2019). Sequential Gaussian Simulation is one of the stochastic methods that can provide different realizations from the same input data. Through this method, the random variables at the grid node are simulated one after another and the simulated results are used as conditional data. This method is implemented according to the following steps:

1. Conduct statistical studies and draw histograms of input data
2. Implement Gaussian transformation on the data
3. Fit a model to the empirical variogram
4. Create a grid and a random path for its nodes
5. Run the kriging method at each node according to all available values (original and simulated) and determine the Gaussian distribution
6. Draw a random (simulated) value from Gaussian distribution
7. Make a sequential simulation for other nodes
8. Perform back transformation for the simulated value to the original attribute space (here a realization is implemented)

To implement another realization, the above steps, points 5 to 8 are repeated (Asghari et al. 2006).

Since replicated realizations match the characteristics of the observed data and have equal probabilities, grid point-by-grid point histograms of realizations can approximate probability distribution functions at a given location (grid point). Thus, the probability of exceeding a fixed threshold can be obtained by computing the absolute frequency of realizations exceeding a certain threshold. This spatially varying empirical probability can be displayed in map form, since it can be valuable for decision-making. Moreover, determining the average for the simulated values at the grid points helps to produce an estimated map of the ‘expected’ value over the domain (E-type or expected value estimate) along with their respective standard deviation.

In this study, based on 100 simulated realizations, the SGS results have been used to produce the following maps (over the same regular grid 1 km x 1 km):

1. The E-Type map based on the mean of the 100 realizations to show the overall distribution of indoor radon values;
2. The probability that radon concentration exceeds the reference value according to the European Union rules.

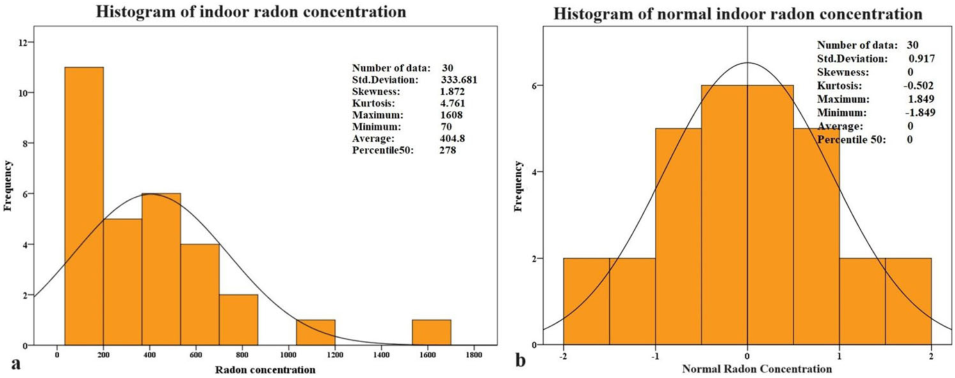

Figure 9. **a** Histograms of indoor radon concentration and **b** normalized indoor radon concentrations with statistical parameters.

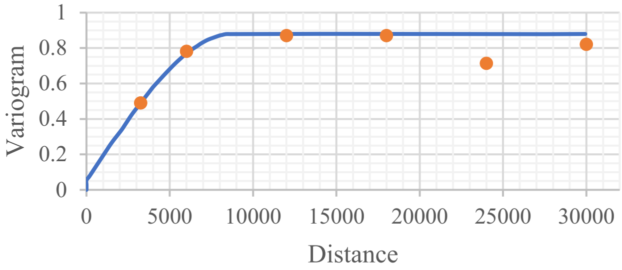

Figure 10. Experimental variogram (points) and fitted model (solid line) of the normal data indoor radon measurements.

Based on the histogram of indoor radon measurements and the summary of statistics shown in Fig. 9a, the indoor radon concentration has varied from 70 Bq/m^3 to 1680 Bq/m^3, and the distribution of values has been positively skewed. The estimated mean indoor radon concentration is 404 Bq/m^3, with approximately 46% of the data showing values higher than this amount. Then before applying SGS, the indoor radon values have been normalized using Gaussian anamorphisms. Figure 9b displays the histogram of indoor radon normalized values, along with a summary of statistical information, respectively.

From the experimental directional variograms of radon data, no anisotropy has been detected; thus, as illustrated in Fig. 10, the following omnidirectional variogram model, with a small nugget effect equal to 0.05, has been fitted:

$$\gamma\,(\mathrm{h}) = 0.05 + 0.84\mathrm{sph}\,(8100), \mathrm{h} \neq 0 \tag{17}$$

where sph(8100) denotes the spherical model with range equal to 8100 m.

Based on the data and the structural analysis, SGS has been conducted to generate 100 realizations on a specific grid. As an example, the SGS maps for the 25th, 50th, 75th, and 100th realizations are presented in Fig. 11. As highlighted in Table 6, there is a close match between some basic statistics determined on the raw data and the ones on the realizations shown in Fig. 11.

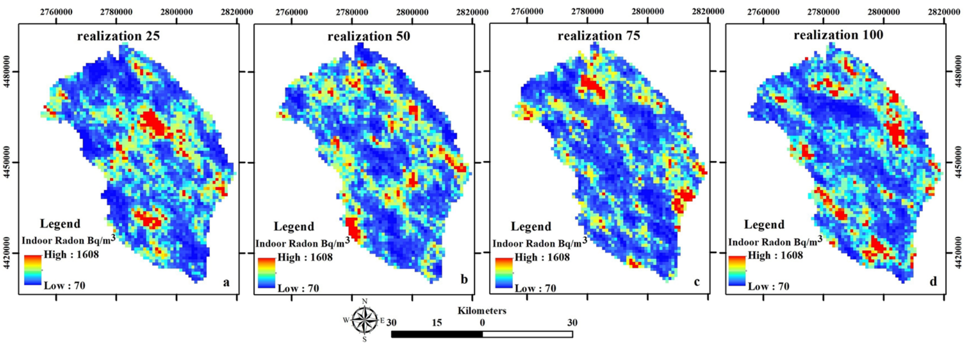

Figure 11. Simulation map of indoor radon measurements, **a** realization 25th, **b** realization 50th, **c** realization 75th, **d** realization 100th.

Table 6. Some statistics on realizations and indoor radon measurements

Statistic parameter	25th	50th	75th	100th	Raw data
Average	401.41	407.74	414.89	404.47	404.80
Min	70	70	70	70	70
Max	1608	1608	1608	1608	1608
Median	295.44	281.49	360.70	256.47	256.00
Standard deviation	314.27	335.29	317.65	345.25	333.68
Count	2760	2760	2760	2760	30

Thus, from the analysis of the 100 conditional realizations, the probability map that the radon concentration exceeds the thresholds 300 Bq/m^3 has been generated as shown in Fig. 12a; thus, areas with a low/high probability of high radon hazard can be identified. These types of maps have practical applications in land management, where they can be employed to pinpoint regions with specific probabilities of health risks or elevated indoor radon concentrations. Also, the E-type map based on the average simulation results in 100 realizations has been produced in order to assess the distribution of radon concentrations in the area under study. The map in Fig. 12b illustrates the variation in radon concentration, ranging between 132 Bq/m^3 and 851 Bq/m^3, along with the indoor radon measurement samples, categorized into two classes: high (> 300 Bq/m^3) and low (≤ 300 Bq/m^3).

Note that the comparison of the final GRHI map ($\gamma = 0.95$) in Fig. 8 with the E-type map in Fig. 12b does not show evident discrepancy in the high radon area potential. Particularly in the southern, northwest, and central regions of the Lecce Province, there is a good alignment between the high radon concentration areas identified by both maps.

4. DISCUSSION AND COMPARISON BETWEEN FGO AND E-TYPE MAPS

Identifying areas with high radon potential is crucial as it enables the implementation of preventive measures to control radon levels and restrict new residential developments

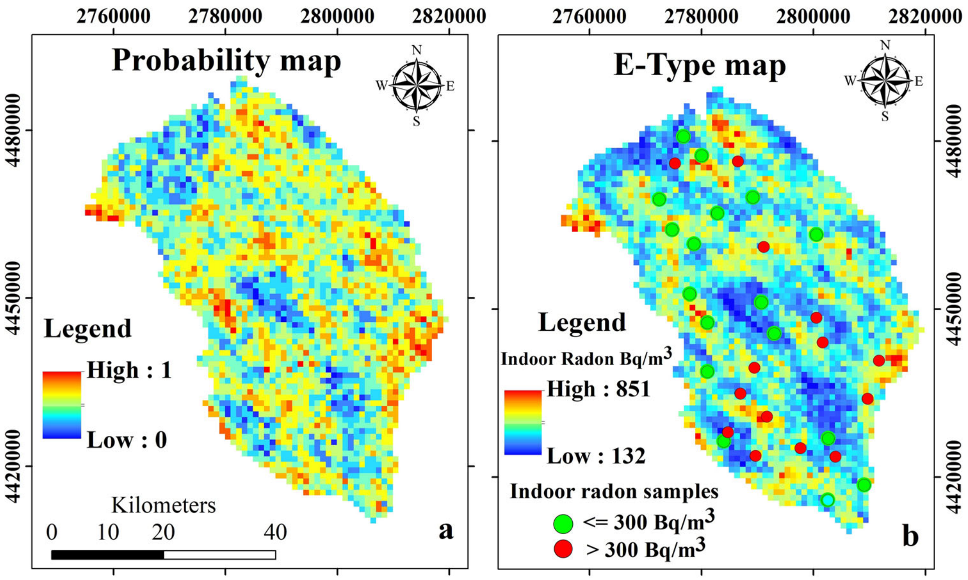

Figure 12. **a** Probability map of occurrence of indoor radon concentration exceeding than 300 Bq/m^3 and **b** E-type map along with indoor radon measurement samples, based on 100 SGS realizations.

in regions with high radon hazard. In particular, understanding the local geogenic radon potential can aid in resource allocation and regulatory focus for effective radon mitigation policies risks. Natural and geogenic factors, such as geological characteristics (rock type and uranium content) and permeability, directly impact radon levels, but other factors like faults, caves, dolines, and sinkholes also play significant roles.

To assess indoor radon hazard and prioritize mitigation efforts, GRHI maps can be produced, as pointed out in many studies (Bossew et al. 2020). In this paper, the AHP was employed to prioritize and assign weights to the crucial criteria, while the FGO method was used to integrate fuzzy maps. Two main criteria, geology and karst features, along with their respective sub-criteria, were considered to identify high radon hazard areas. The weights, assigned to criteria in Table 4, showed that the high uranium content in bedrock and faults, as two sub-criteria in geology, carries the heaviest weights, while the high permeability zone related to the lithotype, sinkholes, and dolines is ranked next. These layers were fuzzified by small and large fuzzy membership functions and were integrated according to FGO method to address anomalies and improve the flexibility and precision of the GRHI maps. Additionally, after creating the first GRHI map for the Lecce Province in Italy using GIS-based spatial analysis based on FGO method, different γ values were considered and ROC curves were employed to choose the best one. The values of GRHI maps, obtained from the FGO method on sub-criteria layers with γ values of 0.65. 0.75, 0.85, and 0.95, were classified according to the ROC curve thresholds. GRHI map with the γ value equal to 0.95 and AUC equal to 0.90 highlighted a good correlation between high radon potential area and their effective factors.

The final GRHI map showed radon changes in direct relation with high density areas of faults, sinkholes, and high content of uranium in basement lithology. A thorough examination of this map clearly indicated that the areas of radon hazard are identified in correlation with the primary faults in the southern part of the province, sinkholes, as well as other sub-criteria such as lithology containing high uranium content and a high level of permeability. According to the ROC curves in Fig. 7 and based on Youden index, two radon hazard classes (high and low) were defined for each γ value. For different γ values, areas of high radon hazard, marked in red, are mostly concentrated in the southern parts. Specifically for $\gamma = 0.95$, there are also some high radon hazard areas in the central and northern parts of the study area, which are compatible with high radon samples (Fig. 8). Regarding lithology, there was evidence of a correlation between the types of outcroppings, especially those categorized as having a high uranium content in bedrock, particularly in limestone and dolomitic–limestone lithology. When overlaying the known geological map (Fig. 1) of the area on the GRHI map (Fig. 8a), a strong concordance was observed. In the southern part of the area, radon levels were classified as higher than in the northeastern part, which confirms the fact that the number of faults and karst features in the latter region is lower than in the other part. Meanwhile, higher indoor radon concentration values were generally linked to faults and karst features. The presence of faults and karst features, mainly oriented in the NW-SE direction, was identified as the most significant contributing factor to the increase in radon concentrations. These geological features also offer potential pathways for the discharge of radon from the deeper layer of the crust.

Furthermore, the method SGS was utilized to generate probability and E-type maps according to 100 simulated realizations. The comparison of the final GRHI map ($\gamma = 0.95$) with the E-type map in Fig. 12b reveals a good alignment in the high radon area potential. Particularly in the southern, northwest, and central regions of the Lecce province, there was a good agreement between the high radon concentration areas identified by both maps. Both the GRHI map, produced using the AHP and FGO methods, and the E-type map share common areas that display a strong association with regions containing faults, sinkholes, and rocks with high uranium content in bedrock. This remark indicates that geological features, such as faults, high uranium content in bedrock, and sinkholes, largely affect the high potential of radon in the identified regions. The presence of faults and high uranium content in bedrock, along with the occurrence of sinkholes, is the primary criteria that contribute to high potential area of radon in these regions as confirmed by the significant effect of karst features in other studies (Botti et al. 2023; Eisenlohr and Surbeck 1995). The results of the study previous study by De Iaco et al. (2017) in this area, which utilized radon in soil gas data alongside other geological and karst feature factors to investigate radon hazard areas, also reveal a good alignment in both final maps. It is noteworthy to mention that this method, grounded in the FGO, identifies radon hazard areas (by using expert judgments, obtained from substantial experience and relevant literature on radon, to weight different criteria and sub-criteria) without relying on sample data. Although the number of indoor radon samples is limited and affects the result of the SGS method, few cases of high radon concentrations identified through this method are not detected by the GRHI method. In these specific local areas, it appears that factors such as dispersion and lower concentration of caves and sinkholes play a notable role. Thus, further investigation of anthropogenic factors is warranted.

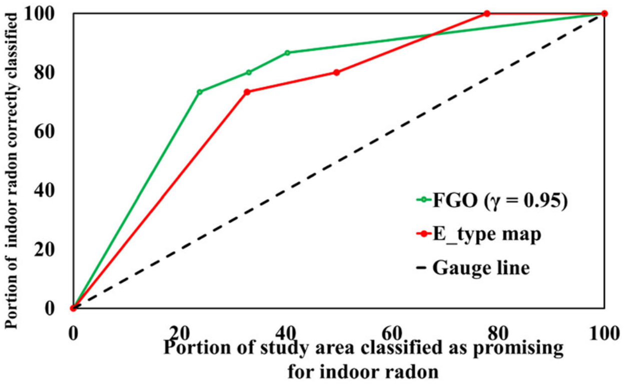

Figure 13. Success rate curves for two GRHI mapping methods.

To evaluate the output maps of the two adopted methods (that is, the FGO map with γ equal to 0.95 and the E-type map), the success rate curve (SRC) approach has been employed. This technique has been widely used in various studies (Parsa et al. 2016; Ghezelbash and Maghsoudi 2018; Carranza and Laborte 2015). The constructed SRC illustrates the portion of study area classified as promising high indoor radon (Pa) along the horizontal axis and the portion of the high radon potential samples predicted correctly (Po) along the vertical axis. To assess the importance and effectiveness of spatial evidence layers in creating radon hazard maps, Parsa et al. (2016) proposed the use of a gauge line, which corresponds to a diagonal line. Positive spatial associations can be determined by comparing the SRC of evidence layers with a gauge line. If the curve is above the gauge line, it indicates a positive association between the evidence layer and its corresponding targets. Conversely, if the curve is below the gauge line, it suggests a lack of positive spatial association. Additionally, it is crucial to plot all success rate curves in the same diagram for a comparative analysis. In this specific case, when the SRC of one method exceeds the one of another, it suggests a stronger spatial correlation with high radon concentration. As described in Agterberg and Bonham-Carter (2005), calculating Pa and Po values and plotting success rate curves require classifying evidential values. In this study, threshold values, derived by using the natural breaks method in QGIS (North 2009) have been employed to classify the final FGO map (with γ equal to 0.95) and the E-type map into ten classes. By using these thresholds and calculating the proportion of the area and the proportion of high radon samples within each threshold, the Pa and Po values for both maps have been plotted. This process has enabled the generation of the success rate curves, as shown in Fig. 13. In particular, the analysis of Fig. 13 reveals that both models effectively delineate promising areas with high potential radon, as their success rate curves are above the diagonal line. Nonetheless, the success rate curve of the FGO method surpasses the gauge line to a greater extent compared to the SGS method, indicating a higher level of success in identifying areas with elevated radon potential.

Since indoor radon concentration can be influenced by human factors including lifestyle, quality of construction of residential areas (cracks in the foundations of buildings caused by ground deformation), then these factors can cause some deviations from the predictions only based on geological and karst features. On the other hand, the use of only indoor radon sampling data cannot highlight in different places the regional effects related to the mentioned factors.

Despite the challenges, the produced GRHI map can be effectively used to estimate radon hazards which allow identifying regions in which remedial action for existing and preventive action for new buildings may be necessary.

5. CONCLUSIONS

In conclusion, this research implemented geostatistical and spatial analysis techniques to assess indoor radon levels and identify areas that display high radon potential in the Lecce Province. The GRHI map was generated by integrating various causal factors, including geological characteristics and karst features, using the AHP and FGO methods. The FGO maps, obtained for different values of the parameter γ (0.95, 0.85, 0.75, and 0.65), were validated against real indoor radon measurements in the study region using ROC curve and classified according to Youden index. Among the different γ values, 0.95 was the best (with an AUC of 0.9 in ROC curve), so that the FGO map with γ value equal to 0.95 was used to produce the classification map based on two different radon hazard categories: low and high. Geostatistical simulation, specifically the SGS, was employed to produce probability and E-type maps relied on some sampled indoor radon concentrations, providing additional insights of potential radon distribution patterns. It should be noted that the correlation between indoor radon and GRHI maps is not perfect because other factors than geogenic ones may also contribute to indoor radon such as human activities, lifestyle, and building materials. Therefore, the absence of anthropogenic factors may introduce limitations in certain cases, warranting continuous radon monitoring and further investigations to account for local deviations. To evaluate the FGO and SGS methods, SCR curves were plotted. The results indicate that both methods perform acceptably above the gauge line. However, it was observed that the SCR of the FGO method surpasses the line more significantly than the SGS method, indicating superior identification of areas with elevated radon potential.

According to the available data, the first produced GRHI map in the Lecce province has highlighted areas with high radon concentrations of concern, aiding decision-makers in implementing preventive measures and effective radon mitigation policies. Nevertheless, a high radon potential map has been created for this specific area, supplementary data regarding soil permeability and soil radioactivity can be also included and studied through other techniques including SMCDA approach and artificial neural networks.

ACKNOWLEDGEMENTS

This research was supported by the National Biodiversity Future Center-NBFC, Spoke 4, Activity 4.1. Funder: Project funded under the National Recovery and Resilience Plan (NRRP), Mission 4 Component 2 Investment 1.4 - Call for tender No. 3138 of 16 December 2021, rectified by Decree n. 3175 of 18 December 2021 of Italian Ministry of University and Research funded by the European Union - Next GenerationEU. Award Number: Project code CN_00000033, Concession Decree No. 1034 of 17 June 2022 adopted by the Italian Ministry of University and Research, CUP F87G22000290001, Project title “National Biodiversity Future Center - NBFC”. We would like to thank the anonymous peer reviewers for their valuable feedback and constructive suggestions, which have significantly improved the quality of this manuscript.

Author Contributions Each of the authors made substantial contributions to the conceptualization and structuring of the research study. Iman Masoumi wrote the original draft. He also collected, analyzed, and validated the data. Sabrina Maggio and Sandra De Iaco were involved in reviewing, editing, and providing supervision for the study. All authors have thoroughly reviewed and endorsed the final, published iteration of the manuscript.

Funding Open access funding provided by Università del Salento within the CRUI-CARE Agreement.

Data Availability Statement Upon request, data will be provided.

Declarations

Conflict of interest The authors assert their declaration that they do not possess any identifiable conflicting financial interests or personal affiliations that might have appeared to exert an influence on the research presented in this manuscript.

[Received December 2023. Revised August 2024. Accepted August 2024.]

REFERENCES

Agterberg FP, Bonham-Carter GF (2005) Measuring the performance of mineral-potential maps. Nat Resour Res 14(1):1–17. https://doi.org/10.1007/s11053-005-4674-0

AlFanatseh A (2022) Land suitability analysis of urban development in the Aqaba area, Jordan, using a GIS-based analytic hierarchy process. GeoJournal 87(5):4143–4159. https://doi.org/10.1007/s10708-021-10488-1

Allen, PA, Allen JRL (2013) Basin analysis: principles and application to petroleum play assessment [Online]. Available https://api.semanticscholar.org/CorpusID:128018140

Angell WJ (2009) WHO Handbook on Indoor Radon: A Public Health Perspective. In: Zeeb, H and Shannon, F (Eds), World Health Organization

Asghari O, Soltni F, Amnieh HB (2006) The comparison between sequential gaussian simulation (SGS) of choghart ore deposit and geostatistical estimation through ordinary kriging. [Online]. Available https://api.semanticscholar.org/CorpusID:59387314

Bekteshi S, Kabashi S, Ahmetaj S, Xhafa B, Hodolli G, Kadiri S, Alijaj F, Abdullahu B (2017) Radon concentrations and exposure levels in the Trepça underground mine: a comparative study. J Clean Prod 155:198–203. https://doi.org/10.1016/j.jclepro.2016.10.131

Beldean-Galea MS, Dicu T., Cucoş A, Burghele B-D, Catalina T, Botoş M, Ţenter A, Szacsvai K, Lupulescu A, Pap I, Dobrei G, Moldovan M, Tunyagi A, Florică Ş, Pănescu V, Sainz C (2020) Evaluation of indoor air pollutants in 100 retrofit residential buildings from Romania during cold season. J Clean Prod 277:124098. https://doi.org/10.1016/j.jclepro.2020.124098

Bossew P, Cinelli G, Ciotoli G, Crowley QG, De Cort M, Medina JE, Gruber V, Petermann E, Tollefsen T (2020) Development of a geogenic radon hazard index-concept, history, experiences. Int J Environ Res Public Health 17(11):4134. https://doi.org/10.3390/ijerph17114134

Botti T, Buresti G, Caricato AP, Chezzi A, Leonardi F, Luzzi L, Trevisi R (2023) Factors affecting indoor radon levels in buildings located in a karst area: a statistical analysis. Atmosphere (Basel) 14(6):950. https://doi.org/10.3390/atmos14060950

Buttafuoco G, Tallarico A, Falcone G, Guagliardi I (2010) A geostatistical approach for mapping and uncertainty assessment of geogenic radon gas in soil in an area of southern Italy. Environ Earth Sci 61(3):491–505. https://doi.org/10.1007/s12665-009-0360-6

Caramanna G, Ciotoli G, Nisio S (2008) A review of natural sinkhole phenomena in Italian plain areas. Nat Hazards 45(2):145–172. https://doi.org/10.1007/s11069-007-9165-7

Carranza EJM, Laborte AG (2015) Random forest predictive modeling of mineral prospectivity with small number of prospects and data with missing values in Abra (Philippines). Comput Geosci 74:60–70. https://doi.org/10.1016/j.cageo.2014.10.004

Čeliković I, Pantelić G, Vukanac I, Krneta Nikolić J, Živanovic M, Cinelli G, Gruber V, Baumann S, Quindos Poncela LS, Rabago D (2022) Outdoor radon as a tool to estimate radon priority areas-a literature overview. Int J Environ Res Public Health. 19(2):662. https://doi.org/10.3390/ijerph19020662

Chen C-Y, Huang W-L (2013) Land use change and landslide characteristics analysis for community-based disaster mitigation. Environ Monit Assess 185(5):4125–4139. https://doi.org/10.1007/s10661-012-2855-y

Cinelli G, Tositti L, Capaccioni B, Brattich E, Mostacci D (2015) Soil gas radon assessment and development of a radon risk map in Bolsena, Central Italy. Environ Geochem Health 37(2):305–319. https://doi.org/10.1007/s10653-014-9649-9

Ciotoli G, Procesi M, Finoia MG, Bossew P, Cinelli G, Tollefsen T, Elìo J, Gruber V (2020) Spatial multicriteria decision analysis (SMCDA) for the construction of the European Geogenic Radon Migration map, EGU General Assembly 2020. https://doi.org/10.5194/egusphere-egu2020-7350

Ciotoli G., Voltaggio M, Tuccimei P, Soligo M, Pasculli A, Beaubien SE, Bigi S (2017) Geographically weighted regression and geostatistical techniques to construct the geogenic radon potential map of the Lazio region: A methodological proposal for the European Atlas of Natural Radiation. J Environ Radioact 166:355–375. https://doi.org/10.1016/j.jenvrad.2016.05.010

Ciotoli G, Lombardi S, Annunziatellis A (2007) Geostatistical analysis of soil gas data in a high seismic intermontane basin: Fucino Plain, central Italy. J Geophys Res 112(B5):B05407. https://doi.org/10.1029/2005JB004044

Clement CH, Tirmarche M, Harrison JD, Laurier D, Paquet F, Blanchardon E, Marsh JW (2010) Lung cancer risk from radon and progeny and statement on radon. Ann ICRP 40(1):1–64. https://doi.org/10.1016/j.icrp.2011.08.011

Coletti C, Ciotoli G, Benà E, Brattich E, Cinelli G, Galgaro A, Massironi M, Mazzoli C, Mostacci D, Morozzi P, Mozzi P, Nava J, Ruggiero L, Sciarra A, Tositti L, Sassi R (2022) The assessment of local geological factors for the construction of a Geogenic Radon Potential map using regression kriging: a case study from the Euganean Hills volcanic district (Italy). Sci Total Environ. https://doi.org/10.1016/j.scitotenv.2021.152064

Cori L, Bustaffa E, Cappai M, Curzio O, Dettori I, Loi N, Nurchis P, Sanna A, Serra G, Sirigu E, Tidore M, Bianchi F (2022) The role of risk communication in radon mapping, risk assessment and mitigation activities in Sardinia (Italy). Adv Geosci 57:49–61. https://doi.org/10.5194/adgeo-57-49-2022

Dai D, Neal FB, Diem J, Deocampo DM, Stauber C, Dignam T (2019) Confluent impact of housing and geology on indoor radon concentrations in Atlanta, Georgia, United States. Sci Total Environ 668:500–511. https://doi.org/10.1016/j.scitotenv.2019.02.257

De Iaco S, Maggio S, Palma M (2017) Radon predictions with geographical information system covariates: from spatial sampling to modeling. Geogr Anal 49(2):215–235. https://doi.org/10.1111/gean.12118

Dobrzyńska MM, Gajowik A, Wieprzowski K (2023) Radon: occurrence and impact on the health. Rocz Panstw Zakl Hig. 74(1):5–14. https://doi.org/10.32394/rpzh.2023.0242

Domenico PA, Schwartz FW (1997) Physical and chemical hydrogeology 2nd Edition, Wiley

Durec F, Hlasny T, Prokesova R (2003) Use of geostatistical analysis in radon mapping. IAEA: Book of abstracts, p. 105

Eisenlohr L, Surbeck H (1995) Radon as a natural tracer to study transport processes in a karst system. An example in the Swiss Jura. [Online]. Available https://api.semanticscholar.org/CorpusID:133062945

Eitvandi N, Sarikhani R, Derikvand S (2022) Landslide susceptibility mapping by integrating analytical hierarchy process, frequency ratio, and fuzzy gamma operator models, case study: North of Lorestan Province, Iran. Environ Monit Assess 194(9):600. https://doi.org/10.1007/s10661-022-10206-5

Elío J, Petermann E, Bossew P, Janik M (2023) Machine learning in environmental radon science. Appl Radiat Isot 194:110684. https://doi.org/10.1016/j.apradiso.2023.110684

Fawcett T (2006) An introduction to ROC analysis. Pattern Recognit Lett 27(8):861–874. https://doi.org/10.1016/j.patrec.2005.10.010

Festa V, Fiore A, Miccoli MN, Parise M, Spalluto L (2015) Tectonics versus Karst Relationships in the Salento Peninsula (Apulia, Southern Italy): Implications for a Comprehensive Land-Use Planning. In: Engineering Geology for Society and Territory - Volume 5, Cham: Springer International Publishing, pp 493–496. https://doi.org/10.1007/978-3-319-09048-1_95

Friedmann H, Baumgartner A, Bernreiter M, Gräser J, Gruber V, Kabrt F, Kaineder H, Maringer FJ, Ringer W, Seidel C, Wurm, G (2017) Indoor radon, geogenic radon surrogates and geology: investigations on their correlation. J Environ Radioact 166:382–389. https://doi.org/10.1016/j.jenvrad.2016.04.028

Ghezelbash R, Maghsoudi A (2018) Comparison of U -spatial statistics and C-A fractal models for delineating anomaly patterns of porphyry-type Cu geochemical signatures in the Varzaghan district, NW Iran. CR Geosci 350(4):180–191. https://doi.org/10.1016/j.crte.2018.02.003

Giglioni V, García-Macías E, Venanzi I, Ierimonti L, Ubertini F (2021) The use of receiver operating characteristic curves and precision-versus-recall curves as performance metrics in unsupervised structural damage classification under changing environment. Eng Struct 246:113029. https://doi.org/10.1016/j.engstruct.2021.113029

Giustini F, Ruggiero L, Sciarra A, Beaubien SE, Graziani S, Galli G, Pizzino L, Tartarello MC, Lucchetti C, Sirianni P, Tuccimei P, Voltaggio M, Bigi S, Ciotoli G (2022) Radon Hazard in Central Italy: comparison among areas with different geogenic radon potential. Int J Environ Res Public Health 19(2):666. https://doi.org/10.3390/ijerph19020666

Giustini F, Ciotoli G, Rinaldini A, Ruggiero L, Voltaggio M (2019) Mapping the geogenic radon potential and radon risk by using Empirical Bayesian Kriging regression: A case study from a volcanic area of central Italy. Sci Total Environ 661:449–464. https://doi.org/10.1016/j.scitotenv.2019.01.146

Giustini F, Procesi M, Finoia M, Sassi R, Mazzoli C, Ciotoli G (2021) Mapping the Geogenic Radon Hazard Index of Italy, EGU General Assembly 2021, online, 19–30 Apr 2021, EGU21-7343. https://doi.org/10.5194/egusphere-egu21-7343

Gruber V, Bossew P, De Cort M, Tollefsen T (2013) The European map of the geogenic radon potential. J Radiol Prot 33(1):51–60. https://doi.org/10.1088/0952-4746/33/1/51

Guida D, Guida M, Cuomo A, Guadagnuolo D, Siervo V (2013) Assessment and Mapping of Radon-prone Areas on a regional scale as application of a Hierarchical Adaptive and Multi-scale Approach for the Environmental Planning. Case Study of Campania Region, Southern Italy. WSEAS Transactions on Systems, 12(2):105–120. https://wseas.com/journals/systems/2013/56-329.pdf

Hsu P-F, Wu C-R, Li Y-T (2008) Selection of infectious medical waste disposal firms by using the analytic hierarchy process and sensitivity analysis. Waste Manag 28(8):1386–1394. https://doi.org/10.1016/j.wasman.2007.05.016

International Commission on Radiological Protection, Protection against radon-222 at home and at work. Pergamon, 1994

Kelley DL (2009) Geochemical Anomaly and Mineral Prospectivity Mapping in GIS. Econ Geol 104(6), 890–890, https://doi.org/10.2113/gsecongeo.104.6.890

Khan AR, Rafique M, Rahman SU, Basharat M, Shahzadi C, Ahmed I (2019) Geo-spatial analysis of radon in spring and well water using kriging interpolation method. Water Supply 19(1):222–235. https://doi.org/10.2166/ws.2018.070

Leucci G, Margiotta S, Negri S (2004) Geophysical and geological investigations in a karstic environment (Salice Salentino, Lecce, Italy). J Environ Eng Geophys 9(1):25–34. https://doi.org/10.4133/JEEG9.1.25

Lewis SM, Fitts G, Kelly M, Dale L (2014) A fuzzy logic-based spatial suitability model for drought-tolerant switchgrass in the United States. Comput Electron Agric 103:39–47. https://doi.org/10.1016/j.compag.2014.02.006

Loffredo F, Scala A, Serra M, Quarto M (2021) Radon risk mapping: a new geostatistical method based on Lorenz Curve and Gini index. J Environ Radioact 233:106612. https://doi.org/10.1016/j.jenvrad.2021.106612

Loffredo F, Opoku-Ntim I, Kitson-Mills D, Quarto M (2022) Gini Method Application: Indoor Radon Survey in Kpong, Ghana. Atmosphere (Basel) 13(8):1179. https://doi.org/10.3390/atmos13081179

Lupiano V, Procopio S, Buttafuoco G, Rago V, Iovine G (2023) Indoor radon measurements in Calabria (Southern Italy). J Maps. https://doi.org/10.1080/17445647.2022.2132883

Malmqvist L, Isaksson M, Kristiansson K (1989) Radon migration through soil and bedrock. Geoexploration 26(2):135–144. https://doi.org/10.1016/0016-7142(89)90058-6

Masoumi I, Maggio S, De Iaco S, Ghezelbash R (2024) Spatial multi-criteria approaches for estimating geogenic radon hazard index. Sci Total Environ. https://doi.org/10.1016/j.scitotenv.2024.176419

Miles JCH, Appleton JD (2005) Mapping variation in radon potential both between and within geological units. J Radiol Prot 25(3):257–276. https://doi.org/10.1088/0952-4746/25/3/003

Mohebbi Tafreshi G, Nakhaei M, Lak R (2021) Land subsidence risk assessment using GIS fuzzy logic spatial modeling in Varamin aquifer, Iran. GeoJournal 86(3):1203–1223. https://doi.org/10.1007/s10708-019-10129-8

Motiee H, Khalili R, Gholami B, Motiee S (2023) A decision making approach for water transfer systems by analytical hierarchy process (AHP) and GIS. Water Resources Manag 37(12):4623–4637. https://doi.org/10.1007/s11269-023-03559-0

Nahm FS (2022) Receiver operating characteristic curve: overview and practical use for clinicians. Korean J Anesthesiol 75(1):25–36. https://doi.org/10.4097/kja.21209

Nazaroff WW (1992) Radon transport from soil to air. Rev Geophys 30(2):137–160. https://doi.org/10.1029/92RG00055

Nefeslioglu HA, Sezer EA, Gokceoglu C, Ayas Z (2013) A modified analytical hierarchy process (M-AHP) approach for decision support systems in natural hazard assessments. Comput Geosci 59:1–8. https://doi.org/10.1016/j.cageo.2013.05.010

Nogarotto A (2018) Mapping the bedrock K2O, U and Th concentration in Italy—Towards the European Atlas of Natural Radiation (Master's thesis, University of Bologna), https://amslaurea.unibo.it/15754/

North MA (2009) A method for implementing a statistically significant number of data classes in the jenks algorithm. In: 2009 Sixth International Conference on Fuzzy Systems and Knowledge Discovery, IEEE, 2009, pp 35–38. https://doi.org/10.1109/FSKD.2009.319

Park N-W, Kim Y, Chang B-U, Kwak G-H (2019) County-level indoor radon concentration mapping and uncertainty assessment in South Korea using geostatistical simulation and environmental factors. J Environ Radioact 208–209:106044. https://doi.org/10.1016/j.jenvrad.2019.106044

Parsa M, Maghsoudi A, Yousefi M, Sadeghi M (2016) Prospectivity modeling of porphyry-Cu deposits by identification and integration of efficient mono-elemental geochemical signatures. J Afr Earth Sc 114:228–241. https://doi.org/10.1016/j.jafrearsci.2015.12.007

Petermann E, Bossew P (2021) Mapping indoor radon hazard in Germany: the geogenic component. Sci Total Environ 780:146601. https://doi.org/10.1016/j.scitotenv.2021.146601

Petermann E, Meyer H, Nussbaum M, Bossew P (2021) Mapping the geogenic radon potential for Germany by machine learning. Sci Total Environ 754:142291. https://doi.org/10.1016/j.scitotenv.2020.142291

Raines GL, Sawatzky DL, Bonham-Carter G (2010) New ArcGIS 10 in fuzzy logic tools. [Online]. Available https://api.semanticscholar.org/CorpusID:35841592

Rezaie F, Panahi M, Lee J, Lee J, Kim S, Yoo J, Lee S (2022) Radon potential mapping in Jangsu-gun, South Korea using probabilistic and deep learning algorithms. Environ Pollut 292:118385. https://doi.org/10.1016/j.envpol.2021.118385

Roumeliotis S, Schurgers J, Tsalikakis DG, D'Arrigo G, Gori M, Pitino A, Leonardis D, Tripepi G, Liakopoulos V (2024) ROC curve analysis: a useful statistic multi-tool in the research of nephrology. Int Urol Nephrol 56:2651–2658. https://doi.org/10.1007/s11255-024-04022-8

Saaty TL, Vargas LG (2013) The Analytic Network Process. In: Decision Making with the Analytic Network Process. International Series in Operations Research & Management Science, 195. Springer, Boston, MA. https://doi.org/10.1007/978-1-4614-7279-7_1

Saaty TL (1977) A scaling method for priorities in hierarchical structures. J Math Psychol 15(3):234–281. https://doi.org/10.1016/0022-2496(77)90033-5

Sciocchetti G, Scacco F, Baldassini PG, Battella C, Bovi M, Monte L (1985) The Italian national survey of indoor radon exposure. Sci Total Environ 45:327–333. https://doi.org/10.1016/0048-9697(85)90234-7

Sekandari M, Masoumi I, Beiranvand Pour A, Muslim AM, Rahmani O, Hashim M, Zoheir B, Pradhan B, Misra A, Aminpour SM (2020) Application of Landsat-8, Sentinel-2, ASTER and Worldview-3 spectral imagery for exploration of carbonate-hosted Pb-Zn deposits in the Central Iranian Terrane (CIT). Remote Sens (Basel). 12(8):1–33. https://doi.org/10.3390/RS12081239

Smethurst MA, Watson RJ, Baranwal VC, Rudjord AL, Finne I (2017) The predictive power of airborne gamma ray survey data on the locations of domestic radon hazards in Norway: A strong case for utilizing airborne data in large-scale radon potential mapping. J Environ Radioact 166:321–340. https://doi.org/10.1016/j.jenvrad.2016.04.006

Szabó KZ, Jordan G, Horváth Á, Szabó C (2014) Mapping the geogenic radon potential: methodology and spatial analysis for central Hungary. J Environ Radioact 129:107–120. https://doi.org/10.1016/j.jenvrad.2013.12.009

Taroni M, Bartolomei P, Esposito M, Vaccaro C (2010) High Radon concentration in the karst area of south Puglia, Italy, [Online]. Available https://api.semanticscholar.org/CorpusID:128929810

Tulipano L, Fidelibus MD (2002) Mechanisms of groundwater salinisation in a coastal karstic aquifer subject to over-exploitation. In: 17th Salt Water Intrusion Meeting DELFT, Delft: Hydrology & Ecology Section, Faculty of Civil Engineering and Geosciences, Delft University of Technology, pp 262–272, ISBN: 90-800089-8-2. Available https://www.researchgate.net/publication/234747522

Youden WJ (1950) Index for rating diagnostic tests. Cancer 3(1):32–35. https://doi.org/10.1002/1097-0142(1950)3:132::AID-CNCR28200301063.0.CO;2-3

Zadeh LA (1965) Fuzzy sets. Inf Control 8(3):338–353. https://doi.org/10.1016/S0019-9958(65)90241-X

Zhang J, Su Y, Wu J, Liang H (2015) GIS based land suitability assessment for tobacco production using AHP and fuzzy set in Shandong province of China. Comput Electron Agric 114:202–211. https://doi.org/10.1016/j.compag.2015.04.004

Zhukovsky M, Yarmoshenko I, Kiselev S (2012) Combination of geological data and radon survey results for radon mapping. J Environ Radioact 112:1–3. https://doi.org/10.1016/j.jenvrad.2012.02.013